

# Chapter 1

## Observations of Quasistatic Fault Growth from Acoustic Emissions

*D.A. Lockner<sup>1</sup>, J.D. Byerlee<sup>1</sup>, V. Kuksenko<sup>2</sup>,  
A. Ponomarev<sup>3</sup>, and A. Sidorin<sup>3</sup>*

<sup>1</sup>*U. S. Geological Survey, 345 Middlefield Rd., Menlo Park, CA 94025,  
U. S. A.*

<sup>2</sup>*A. F. Ioffe Physical-Technical Institute, Russian Academy of Sciences,  
Polytechnicheskaya 26, St. Petersburg, Russia 194021.*

<sup>3</sup>*Institute of Physics of the Earth, Russian Academy of Sciences,  
Bolshaya Gruzinskaya 10, Moscow D-242 Russia 123810.*

### Abstract

The location of acoustic emission (AE) sources during deformation of rock has proven to be a useful non-destructive analytic technique. We present experimental results, based on AE observations, that show the nucleation and growth of macroscopic fault planes in granite and sandstone samples. By controlling axial stress to maintain constant AE rate rather than more conventional loading conditions such as constant strain rate or constant stress, we have been successful in retarding the failure process in triaxial experiments. As a result, the post-failure stress curve has been followed quasistatically, extending to minutes or hours the fault growth process that normally would occur violently in a fraction of a second. In addition to this novel control system, three-dimensional locations of AE events were determined by analyzing the relative arrival times of AE pulses recorded on a network of transducers attached to the sample. In this manner, as many as 40000 AE events were located in the course of a single experiment.

While the details of fault formation varied from experiment to experiment, a number of features were consistently observed. In all three granite experiments, the fault plane nucleated abruptly at a point on the sample surface soon after reaching peak stress. Prior to fault nucleation, microcrack growth was distributed evenly throughout the granite samples. From the nucleation site, the fault plane grew across the sample, accompanied by a gradual drop in axial stress. AE locations showed that the fault propagated as a fracture front (process zone) with in-plane dimension of 10-50 mm. As the fracture front passed, the AE from a given region would drop to a low level. If allowed to progress to completion, stress eventually dropped to the frictional sliding strength. Sandstone samples showed somewhat

different response. In these experiments, a diffuse damage zone appeared prior to peak strength and gradually localized into an incipient fault plane. After passing through peak stress, this plane grew, as in the granite samples, to eventually bisect the sample.

## 1. Introduction

It is well known that brittle rocks, when loaded in compression, will commonly fail by the development of a large-scale fault. The growth of such a fault results in an overall weakening of the rock and is usually accompanied by a violent release of energy (earthquake). It is surprising that, while this mode of failure has been studied in detail for many years (Jaeger and Cook, 1984), the details of how faults nucleate and grow have remained an enigma for so long. This situation is due in part to the tendency for faults to grow at near shear wave velocity, making the detailed observation of fault propagation technically difficult. It is also due to the lack of an adequate theory of how faults can grow in-plane.

In the past, experiments designed to investigate the fracture development or 'post failure' stage in the brittle failure process have resorted to 'stiff' loading frames (Wawersik and Fairhurst, 1970; Wawersik and Brace, 1971; Wong, 1982a,b). By reducing the amount of elastic energy available to the sample during fault formation, this approach can greatly increase stability. Even so, many crystalline rocks such as Westerly granite store sufficient energy in the sample itself to drive unstable fault growth. In this case, the loading system must be fast enough to actively remove energy from the system as the fault grows. We present here an experimental technique in which the rate of acoustic emissions (AE) occurring in the sample is used to control axial stress. This system, similar to one employed by Terada et al. (1984), has proven capable of arresting unstable fault growth so that it can be observed under quasistatic growth conditions. Then, by recording the relative arrival times of AE signals at transducers mounted on the sample, we are able to locate the microcrack damage that occurs during the faulting process. In this manner, information concerning the complete nucleation and growth history is obtained.

When deformed samples of brittle rock are examined in thin section and with SEM (Hadley, 1975; Tapponnier and Brace, 1976), microcrack damage is found to be dominated by the growth of mode I tensile cracks that are subparallel to the maximum compressive stress direction. On the microscopic scale, mode I crack damage is consistently favored over shear failure modes, indicating that tensile fracture toughness is lower than shear fracture toughness in this class of materials. These observations are supported by elastic crack theory, which predicts that cracks will tend to grow in mode I towards the direction of maximum compressive stress (Lawn and Wilshaw, 1975). Since faulting is consistently observed on the macroscopic scale, considerable effort has gone into bridging the gap between pre-faulting microscopic damage and the coalescence of damage needed to form a fault. Models for fault development typically assume that microcracks at first do grow parallel to the direction of maximum compression, and in so doing transfer stress from weakened zones to their surroundings (Madden, 1983). This process continues until the increased crack density ultimately causes cracks to interact, leading to a mechanical instability (e.g., Horii and Nemat-Nasser, 1985; Sammis and Ashby, 1986; Costin, 1987; Lockner and Madden,

1991a,b). Based on the observations presented here, Reches and Lockner (1990) develop a coherent analysis of the process by which microcracks organize themselves to form a fracture plane, while a similar treatment was recently presented by Du and Aydin (1991).

Considerable discussion has been devoted in the literature to the question of when, during the loading cycle of an initially intact rock, the incipient fracture plane can be recognized. Experimentally, researchers have undertaken the laborious task of loading samples to different stages of deformation and then counting microcrack damage in thin section or using SEM techniques (Wawersik, 1973; Hadley, 1975; Tapponnier and Brace, 1976). Using an argillaceous quartzite, Hallbauer et al. (1973) reported the localization of microcrack damage onto an incipient fracture plane as between 95% and 98% of (preceding) peak strength. By means of a holographic technique, Spetzler et al. (1981) reported localized surface dilatancy preceding peak strength by 2% in a pyrophyllite sample. Lockner and Byerlee (1977a) reported that localization of AE sources onto the eventual fault plane occurred in one triaxially loaded Weber sandstone sample at 95% failure strength. However, in a second sandstone sample and two Westerly granite samples, no localization occurred prior to failure. In this paper, we will show examples of faulting in initially intact granite in which nucleation occurs suddenly and after peak strength. In sandstone samples, however, microcrack localization occurs during early loading, presumably as the result of preexisting flaws in the sample. This aspect of the current experiments is analyzed in detail in Lockner and Byerlee (1992a,b) and Lockner et al. (1992). Providing a coherent explanation of these various observations is important if we are to fully understand the brittle fracture process.

An understanding of this fracture process in rock is of obvious importance to our understanding of earthquakes and to our ability to predict earthquakes. This problem can be divided into three classes: long-, intermediate- and short-term predictions. Successful prediction on these time scales has different utility to the public and also requires different types of observations and analysis. To date, long-term predictions have met with the most success by making use of, for example, historical earthquake data, trenching and long-term geodetic strain and tidal data. The success rate for short-term prediction, in which earthquakes are anticipated by a few days or less, has been far worse. This area of research has undergone repeated cycles of optimism and discouragement as various prediction schemes have gained attention and then failed under further testing. A recent example of optimism is the observation of ultra-low-frequency electromagnetic noise prior to the Loma Prieta earthquake of October 1989 (Fraser-Smith et al., 1990).

An important set of borehole strain observations has now been compiled that relates to short-term prediction. Sacks-Everton dilatometers have recorded variations at the nanostrain level or better in the near-field of a number of moderate earthquakes (Johnston et al., 1987; Linde and Johnston, 1989). In no case has precursory strain been observed over a timescale of days to seconds before any of these earthquakes. Owing to the high sensitivity of these instruments, the investigators conclude that any precursory strain that did occur on the eventual rupture plane must have been less than 0.1% of the coseismic strain release. Stated differently (Johnston, 1990), they conclude that short-term precursory strain preceding some of these moderate-sized earthquakes would have been observable if it had occurred on a fault patch larger than about 100 m in dimension. How much smaller the regions that underwent precursory strain actually were remains an open question. This important result has obvious implications for the problem of short-term earthquake prediction. Any plausible short-term prediction

scheme that has been proposed can ultimately be related to strain changes in the earthquake source region. Knowledge of the volume of rock that can be expected to deform will guide us in our estimates of the magnitude of the precursory signals that can be detected remotely.

The experiments presented here are conducted on samples in which faults can grow to approximately 0.1 m in dimension. Thus, just as the borehole dilatometer observations can be used to place an upper bound on the nucleation patch size for earthquakes, we anticipate that our laboratory observations will allow us to place a lower bound on the nucleation size. In one sense, the initially intact samples that are deformed in these experiments could be considered an analog of a stuck patch or asperity on a yielding fault plane. Breakage of such an asperity could represent the initiation of an earthquake. While the samples used in the present experiments were chosen to be homogeneous, future experiments are planned to study the effects of preexisting faults as well as samples with strength heterogeneities. In the present experiments we are able to observe not only the nucleation of fractures, but we will also show that, for the first time, we can monitor the growth phase of fractures as they propagate quasistatically in-plane. Through this new technique, it should also be possible to analyze the energetics of fault propagation (Lockner et al., 1991) to determine the conditions in the earth that will lead to unstable earthquake rupture as well as the arresting phase that terminates earthquakes.

## 2. Experimental

### 2.1. Sample assembly and loading conditions

Cylindrical samples of Westerly granite and Berea sandstone (18% porosity) were prepared. Sandstone samples were cored perpendicular to bedding. Sample dimensions were 76.2 mm diameter by 190.5 mm length. Ends were ground parallel to  $\pm 0.05$  mm. Samples were jacketed in either a 0.38 mm walled copper sleeve or a 3.2 mm thick polyurethane tube (Figure 1). A set of six piezoelectric transducers (resonance at 0.6 MHz) were attached to the sample and used to monitor high-frequency acoustic emission (AE) occurring in the rock as it was deformed. In all experiments a constant confining pressure of  $50 \pm 0.2$  MPa was maintained by computer control. Axial load on the sample was measured with an internal load cell to a precision of  $\pm 0.2$  MPa.

A pulse counter was connected to the amplified output of one of the piezoelectric transducers. This counter generated an output voltage that was proportional to the AE rate occurring in the sample. By including this device in the feedback loop for the axial load, experiments could be run at constant AE rate. A similar system was tested by Terada et al. (1984) in which they employed a computer to condition the AE signal instead of the simple analog device used here. At low differential stress, when there was little AE activity, we adjusted the loading system to provide an axial shortening rate between 0.1 and 1.0  $\mu\text{m s}^{-1}$ . As the load increased, this rate would drop, requiring repeated adjustments during the early stages of each experiment. With increasing stress and therefore increasing AE activity, the control system was designed to maintain an approximately constant acoustic emission rate by reducing, or reversing when necessary, the axial strain rate. In this manner, we were able to monitor the growth of the fracture plane under quasistatic conditions; typically extending the fault formation phase so that it would last a matter of minutes or even hours. In the early stages of fault growth, it

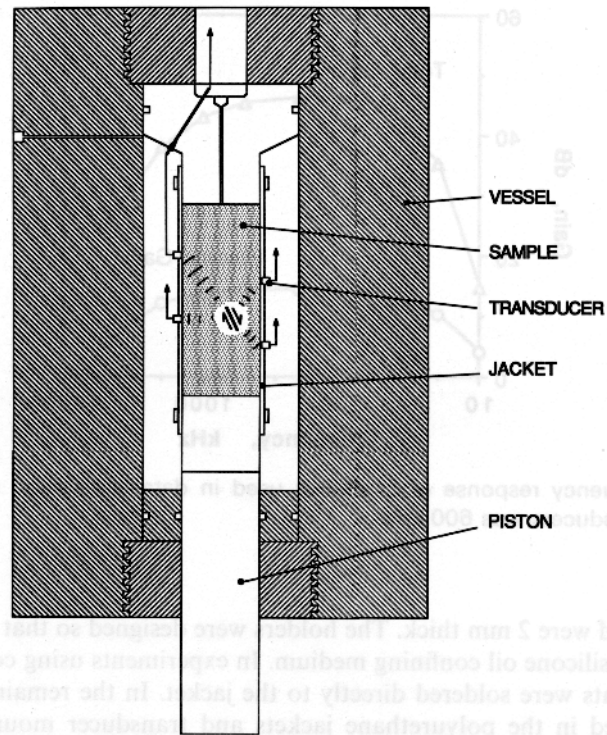


**Figure 1.** Schematic view of sample mounted in pressure vessel. Six piezoelectric transducers mounted on sample surface detected acoustic emissions during deformation. An additional set of four transducers was used to determine velocity field.

was necessary to drop stress rapidly. To accomplish this, axial load was controlled by a fast-acting hydraulic valve with an overall system response of approximately 0.2 Hz. The hydraulic valve was capable of lowering axial stress at a maximum rate of  $6 \text{ MPa s}^{-1}$ . This unloading rate was sufficient to prevent unstable fault growth in all experiments.

Axial shortening of the sample column was measured outside the pressure vessel with a DCDT displacement transducer. Accuracy and sensitivity were, respectively,  $\pm 5 \times 10^{-3} \text{ mm}$  and  $\pm 0.3 \times 10^{-3} \text{ mm}$ . In selected experiments circumferential strain was measured with a single  $40 \text{ mm}^2$  foil strain gage applied to the sample mid-plane. In addition, axially oriented strain gages were mounted on some of the samples. Gage sensitivity was  $\pm 1 \times 10^{-6}$  for short time intervals; however, thermal drift resulted in a long-term stability of  $\pm 5 \times 10^{-6}$ . In the two experiments (referred to as G1 and S1) that used copper jackets, gages were cemented on the jacket. In all other experiments, gages were cemented to the rock surface, underneath the polyurethane jacket.

## 2.2. Acoustic emission monitoring system

A set of six piezoelectric transducers were attached to the sample (shown schematically in Figure 1) to detect ultrasonic noise radiated during the sudden growth of microcracks or slip along existing crack surfaces. The transducers, which were 6.4 mm diameter, were mounted in brass holders whose bottom faces were machined to the radius of curvature

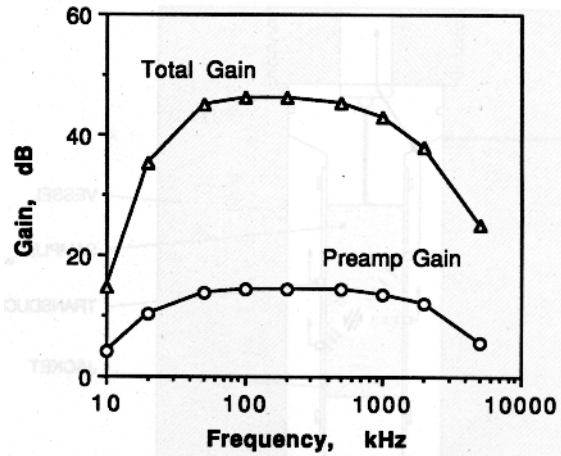


**Figure 2.** Frequency response of amplifiers used in data acquisition system. Resonant frequency of transducers was 600 kHz.

of the sample and were 2 mm thick. The holders were designed so that transducers were immersed in the silicone oil confining medium. In experiments using copper jackets, the transducer mounts were soldered directly to the jacket. In the remaining experiments, holes were drilled in the polyurethane jackets and transducer mounts were epoxied directly to the sample surface. Transducer signals were brought out of the pressure vessel to a set of wide-band preamplifiers (amplifier response is shown in Figure 2). Signals were amplified by 45 db and sent to a six-channel data acquisition and recording system.

The data acquisition system digitizes the relative arrival time of the AE signal at each of the six transducers, the absolute time of arrival of the signal at the transducer nearest the source, the sign (positive or negative) of the first maximum in the wave train at each transducer, the amplitude of the first maximum in the wave train at each transducer, and the maximum amplitude of the wave train seen by any of the transducers during an entire AE event. Arrival time, as determined by the system, is the time when the input signal first exceeds a preset threshold level and is recorded to  $\pm 0.05 \mu\text{s}$  accuracy. A discussion of the location accuracy of this acquisition system appears in the appendix. Amplitudes are stored as integer values on a linear scale from 2 to 99 (over-range events are recorded as 99). Calibration of the system showed that this internal scale corresponds to a range, as referred to transducer output, of 1.0-17.8 mV, to provide a dynamic range of 1.25 decades. The acquisition system can buffer data from up to 32 AE events for a short-term repetition rate of 25 kHz. Data are stored for later analysis by writing blocks of 16 events to magnetic tape. Throughput rate for sustained AE activity is limited by the tape transfer rate to 300 events/s. In the experiments presented here, load on the sample was adjusted dynamically to maintain constant AE rate. This rate was set to  $<100$  events/s, so that events would not be lost as a result of system saturation. Electromagnetic noise will occasionally trigger the acquisition system and will typically appear as coincident arrivals on two or more inputs. To eliminate this noise, the acquisition system automatically rejects events for which the apparent shortest travel time is identical for two stations. Additional details of the data acquisition system are given in Byerlee and Lockner (1977).

### 2.3. Location procedure

The primary use of the AE data is in determining time and three-dimensional position of microseisms to determine where damage is occurring in the sample. To accomplish this task, we treat the six transducer array as a miniature seismic network and invert the relative arrival time data for hypocentral location and event time. In past experiments (e.g., Lockner and Byerlee, 1977a), we inverted arrival time data for velocity as well as time and position. With only six arrival times and five unknowns, there was little redundancy in that inversion procedure. The situation is actually even more serious owing to P-wave anisotropy that develops as the sample is deformed. At the large differential stresses that occur in these experiments, microcracks tend to open parallel to the maximum compressive principal stress direction (along the sample axis). These oriented cracks produce a severe velocity anisotropy (often exceeding 40%) which varies during the course of an experiment (Lockner et al., 1977; Lockner and Byerlee, 1980). In the present experiments, we added an independent set of four piezoelectric transducers to the sample assembly. By driving one transducer with an externally generated 100 V pulse, and measuring the transit time to the three receiving transducers, we were able to determine the P-wave velocity for declinations from the sample axis of 31°, 50° and 90°. From these measurements we determined the mean velocity field in the sample, assuming radial symmetry and an ellipsoidal field. Velocities were measured in this manner between five and eight times during each experiment to determine how the velocity field varied with time. By supplying the velocity to the inversion routine as a known parameter, we have significantly increased the accuracy of the source location determinations.

In seismic inversions, stations are often located on a plane (earth's surface), leading to a reduced resolution of hypocentral depth. In our case, however, transducers are close to AE sources and completely surround them, providing us with good spatial resolution in all directions and making the inversion routine quite robust. We employ a least-squares technique to estimate hypocentral locations by minimizing the travel time residuals. Since the technique is nonlinear, AE locations are determined iteratively by successively improving the hypocentral estimate. When accurate arrival times are provided, the inversion routine generally requires four to six iterations to come within 0.5 mm of the optimum solution. The procedure is similar to that described in Lockner and Byerlee (1980) with the modification that velocities are not solved for, since they are measured independently during each experiment. We will denote our estimate of the source parameters by  $\mathbf{m} = [T_e, X_e, Y_e, Z_e]$ , the time and space coordinates of the AE event. Next, parameters are defined that are related to the travel path to the  $i$ th transducer. These include

$(x, y, z)_i$	coordinates of $i$ th station
$d_i$	distance from AE event to $i$ th station
$\phi_i$	the declination of the travel path relative to the sample axis
$v_i$	average P-wave velocity along travel path to $i$ th station
$t_i$	observed arrival time at $i$ th station
$t_i^m$	estimated arrival time = $T_e + d_i/v_i$ as predicted by model parameters
$R_i$	$t_i - t_i^m$ , travel time residual.

The velocity field in the sample is assumed to be homogeneous. While this can be achieved during the early portions of the experiment by careful choice of sample, the

progressive deformation of the sample invariably leads to velocity field heterogeneity. One problem is the mismatch in elastic modulus between the sample and steel endplugs. The steel plugs tend to provide lateral support for the ends of the sample, retarding the dilatancy and therefore the velocity anisotropy in these regions. The contrast in modulus between rock and steel also creates zones of high shear stress which may influence the mode of failure in the sandstone experiments. However, in all three granite samples tested, end effects appeared to have little effect on fracture initiation since initiation consistently occurred in the central region of the sample. An additional source of velocity heterogeneity is the development of the fault plane itself. This effect will be most severe for ray paths traveling along the fault plane. Clearly, a detailed knowledge of the spatial velocity variation would be desirable. However, obtaining this information is beyond our present capabilities and, for now, we must be satisfied with the assumption of homogeneity. This assumption should be reasonable for events located in the central region of the sample but will lead to systematic location biases for events occurring near the sample ends. This bias will, however, have little effect on relative locations of events occurring near each other. This is an important distinction, since relative location accuracy is the most important for the present analysis. We make the further assumption that the velocity field can be represented by a radially symmetric ellipsoid. Given the loading symmetry, this is a reasonable first approximation, although the preceding discussion on heterogeneity suggests that there are also errors associated with this assumption. The velocity anisotropy is then expressed as  $\zeta = v^{\text{transverse}}/v^{\text{axial}}$ , and generally decreases from 1 to less than 0.7 as the sample is loaded.  $v_i$  is then expressed as

$$v_i/v^{\text{axial}} = \frac{\zeta}{(\sin^2 \phi_i + \zeta^2 \cos^2 \phi_i)^{1/2}}$$

which is equivalent to

$$\frac{1}{v_i} = \left[ \left( \frac{\sin \phi_i}{v^{\text{transverse}}} \right)^2 + \left( \frac{\cos \phi_i}{v^{\text{axial}}} \right)^2 \right]^{1/2}$$

The model adjustment vector  $\delta \mathbf{m}$  is calculated by a linearized least-squares procedure which minimizes  $\|\mathbf{R}\|^2 = \mathbf{R}^T \cdot \mathbf{R}$  where  $\mathbf{R}^T = \mathbf{R}$ -transpose. Then the updated model at the  $k + 1$  step is given by  $\mathbf{m}^{k+1} = \mathbf{m}^k + \delta \mathbf{m}^k$ . The adjustment vector is determined by solving the normal equations

$$\mathbf{A} \delta \mathbf{m} = \mathbf{b}$$

$\mathbf{A}$  and  $\mathbf{b}$  are constructed according to the least-squares formulation from

$$\mathbf{A} = \mathbf{P}^T \mathbf{P}$$

and

$$\mathbf{b} = \mathbf{P}^T \mathbf{R}$$

where  $\mathbf{P}$  is the matrix of partial derivatives given by  $P_{ij} = \partial R_i / \partial m_j$ . In expanded form, elements of  $\mathbf{P}$  are expressed as

$$\begin{aligned} \frac{\partial R_i}{\partial m_1} &= 1, & \frac{\partial R_i}{\partial m_2} &\cong \frac{(X_e - x_i)v_i}{d_i(\zeta v^{\text{axial}})^2} \\ \frac{\partial R_i}{\partial m_3} &\cong \frac{(Y_e - y_i)v_i}{d_i(\zeta v^{\text{axial}})^2}, & \frac{\partial R_i}{\partial m_4} &\cong \frac{(Z_e - z_i)v_i}{d_i(v^{\text{axial}})^2} \end{aligned}$$

The  $\pm 0.05 \mu\text{s}$  arrival time resolution of the data acquisition system sets a limit of about  $\pm 0.4 \text{ mm}$  for the accuracy of determining source locations. However, in practice, other measurement errors further degrade the location accuracies. The primary source of error is a tendency to systematically pick arrivals late for low-amplitude emergent waveforms (Lockner and Byerlee, 1978; also see discussion in appendix), although large-amplitude events are much less affected by this problem. As a result, we estimate that location precision for large-amplitude AE events used in the present analysis is  $\pm 3 \text{ mm}$ . This estimate is confirmed by the tightness of clusters of AE event locations from events occurring on fault planes during the experiments. As mentioned earlier, errors in determining the true velocity field will result in a systematic spatial bias in hypocentral determinations. However, this bias will not have a significant effect on the relative locations of neighboring AE events.

### 3. Results

Differential stress ( $\sigma_d = \sigma_{axial} - P_{conf}$ ) and strain components are plotted in Figure 3 for granite samples G1, G2, G3 and Figure 4 for sandstone samples S1 and S2. Horizontal axis in all plots is the calculated axial shortening of the sample,  $dz$ . Since remote axial displacement  $dz_r$  is measured outside the pressure vessel, it includes both the sample shortening and an additional component of elastic shortening of the steel piston. Thus the sample shortening is computed from

$$dz = dz_r - \frac{\sigma_d}{k}$$

where  $k = 205 \pm 5 \text{ MPa mm}^{-1}$  for the sample assembly used in these experiments. In all three granite samples, fault nucleation was accompanied by an abrupt reversal in slope of the stress-displacement curve soon after peak stress. As the AE locations will show, the post-peak weakening curve corresponds to propagation of the macroscopic fault plane across the sample. In experiments G1, S1 and S2 (Figures 3a, 4a,b), the fracture surface cuts across the sample, just grazing the steel endplug. Once the fault plane has completely bisected the sample in these experiments, further deformation involves slip along the entire fault surface at  $\sigma_d \sim 150 \text{ MPa}$  or a coefficient of friction of approximately 0.75. In experiments G2 and G3, however, the fracture plane initially formed at an angle of  $20\text{-}25^\circ$  and rotated, as it grew, to form an even smaller angle with the sample axis. As a result, in these two experiments the fault intersected the steel endplug, preventing complete loss of strength. In experiment G1 (Figure 3a), the shallow ramp halfway down the weakening curve occurred when the displacement control system was briefly turned off to conduct a velocity measurement. The sample underwent accelerating creep during this period. In all five experiments, the post-peak weakening curve has positive slope and indicates that all of these samples stored sufficient elastic energy to form a through-going fracture surface and would have fractured unstably during a conventional deformation experiment.

Details of the peak strength regions of experiments G1, G3 and S2 are shown in Figure 5 (plotted at 1 s intervals). The episodic stress drops and recoveries are the result of short bursts of AE activity. Since the displacement feedback system attempts to maintain constant AE rate, sudden acoustic bursts result in a rapid unloading of the system. In experiment G1, at least two episodes of incipient fault nucleation occurred

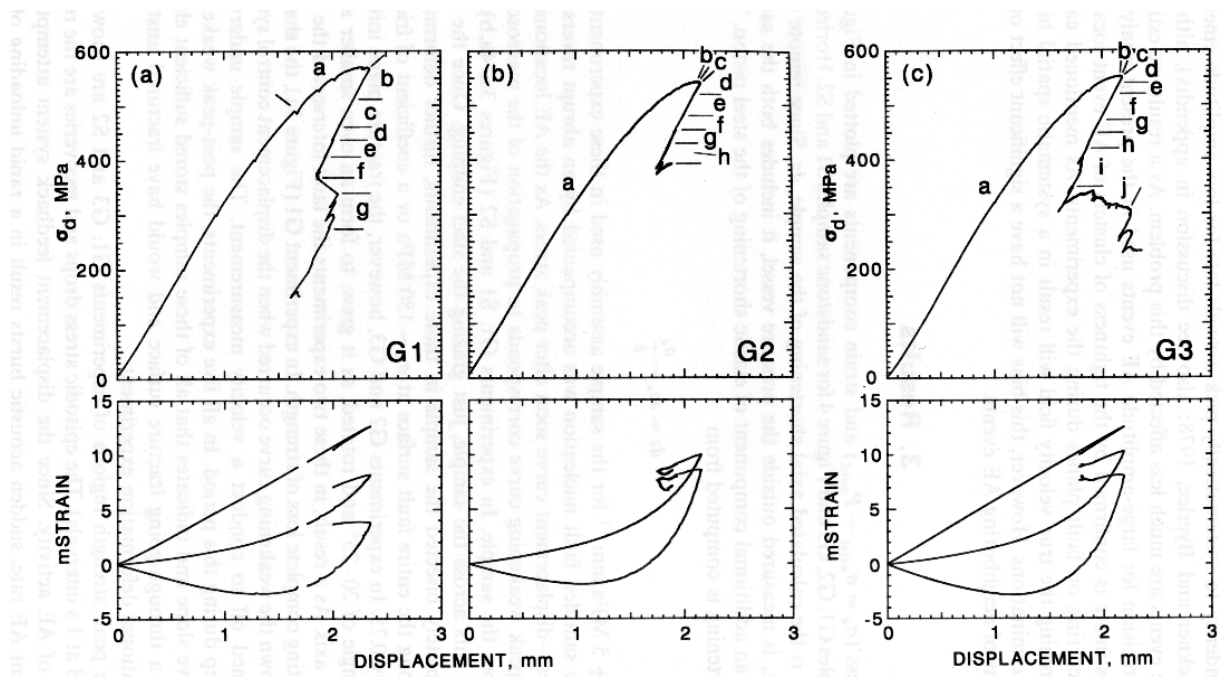


**Figure 3.** Differential stress and strain components plotted as a function of axial shortening of sample (corrected for elastic shortening of loading system). (a) Westerly granite sample G1 ; (b) granite sample G2; (c) granite sample G3. All experiments conducted at 50 MPa confining pressure. Regions indicated on stress curves correspond to AE location plots in Figures 7-9.

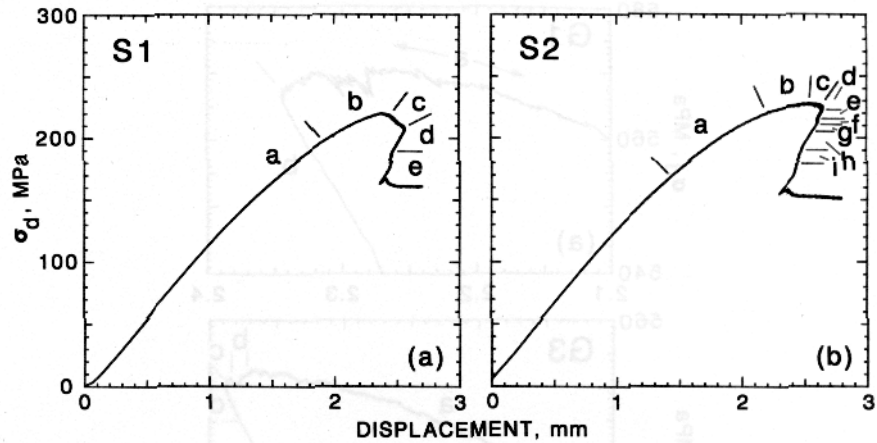


**Figure 4.** Differential stress plotted as a function of axial shortening of sample (corrected for elastic shortening of loading system). (a) Berea sandstone sample S1; (b) sandstone sample S2.  $P_{conf} = 50$  MPa. Regions indicated on stress curves correspond to AE location plots in Figures 10 and 11.

that apparently were arrested before they could go unstable. Similar behavior can be seen for sample G3 which was conducted at a lower AE rate than G1. The sandstone samples also showed short-term stress variations due to bursts of AE events. However, as shown in Figure 5c, the character of the resulting stress-displacement curve differed from that of the granite runs. This difference is mainly the result of the larger number of AE events that occurred in the peak strength region of the sandstone experiments (see Table 1). Between 10 and 30 times as many events were recorded in this region in the sandstone experiments as in the granite. As a result the peak stress region was traversed more slowly in the sandstone experiments. The strength loss that occurred just after the reversal in slope of the stress-displacement curve was also more gradual in the sandstone experiments.

In Figure 6 we show two examples of the P-wave velocity structure used in the hypocentral location program. Solid symbols are measured velocities and open symbols are the inferred axial and transverse velocities. Both the granite and sandstone show an increase in  $v^{axial}$  with initial loading. With the onset of dilatancy about mid-way through the loading curve,  $v^{axial}$  begins to decrease in the granite but not in the sandstone. Following the onset of dilatancy,  $v^{trans}$  drops dramatically in both the granite and sandstone, leading to a pronounced velocity anisotropy by the time of fracture initiation. The granite data are in good agreement with earlier determinations of velocity variations due to deviatoric stress (Lockner et al., 1977). By the end of the fault formation process and the accompanying partial unloading of the sample, both  $v^{axial}$  and  $v^{trans}$  have decreased, although significant anisotropy remains. Return to isotropic loading results in a permanent decrease in P velocity of 10-15% as well as a dramatic loss of anisotropy for both granite and sandstone.

### 3.1. Fault formation in granite

In Figure 7 we present the locations of the largest-amplitude AE events recorded during experiment G1. Each set of events is plotted from three perspectives. In the bottom

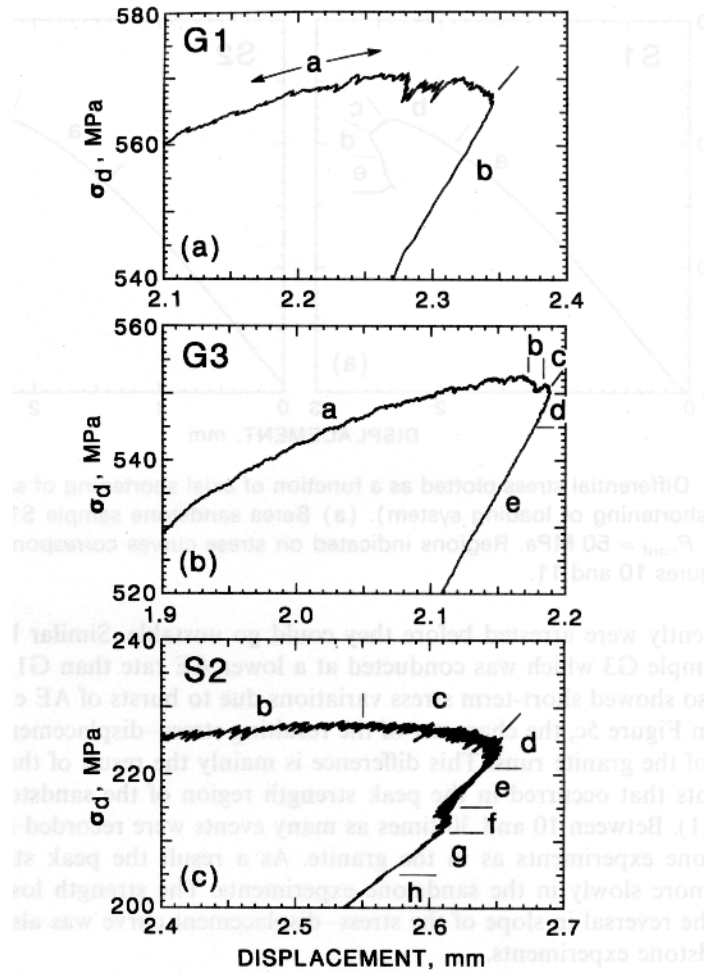


**Figure 5.** Detailed stress-displacement plots of peak stress regions in (a) exp. G1; (b) exp. G3; (c) exp. S2. Regions indicated on stress curves correspond to AE location plots in Figures 7, 9 and 11.

projection of each set the sample is viewed along strike, while in the middle plot the sample has been rotated 90° counterclockwise on its axis to view the fault plane face-on. In the upper plot, the same events are viewed looking down on the sample. Each dot represents one AE event. A summary of the data presented in Figures 7-11 is presented in Table 1. For reference, the projection of the surface trace of the final fault plane is shown in Figure 7a. Since the faults that developed in all experiments were curved to varying degrees, the surface traces drawn in this and subsequent plots can only be used as an approximate indication of the three-dimensional faults. The individual segments of experiment G1 shown in Figure 7a-g are indicated on the stress-displacement curve shown in Figures 3a and 5a.

AE events recorded during the dilatant stage through peak stress in sample G1 are plotted in Figure 7a. Note that events are distributed throughout the central portion of the sample, reflecting the uniform dilatancy occurring during this portion of the

**Table 1.** Summary of AE data

Sample	Figure	Number of events	Start of plot <sup>a</sup> interval (s)	Plot interval (s)	Initial faulting angle [deg]
G1	1.7a	867	-18450	18450	18±3
	1.7b	205	0	100	
	1.7c	443	100	200	
	1.7d	965	300	500	
	1.7e	1360	800	500	
	1.7f	618	1300	1000	
	1.7g	2103	2300	600	
		6561			
G2	1.8a	235	-7900	7700	25±3
	1.8b	16	-200	100	
	1.8c	20	-100	100	
	1.8d	72	0	100	
	1.8e	383	100	200	
	1.8f	412	300	400	
	1.8g	587	700	800	
	1.8h	2565	1500	9000	
		4290			
G3	1.9a	403	-10800	10600	22±3
	1.9b	35	-200	100	
	1.9c	36	-100	100	
	1.9d	50	0	100	
	1.9e	159	100	100	
	1.9f	695	200	200	
	1.9g	786	400	1000	
	1.9h	1691	1400	2000	
	1.9i	5102	3400	4000	
	1.9j	10000	7400	10000	
			18957		
S1	1.1 Oa	1529	-29300	14100	35±3
	1.1 Ob	3808	-15200	7900	
	1.1 OC	7574	-7300	7300	
	1.1 Od	1790	0	2300	
	1.1 Oe	6559	2300	8300	
		21260			
S2	1.11a	830	-53000	10000	33±3
	1.11b	2431	-43000	8000	
	1.11C	3592	-35000	10000	
	1.11d	2733	-25000	10000	
	1.11e	3020	-15000	10000	
	1.11f	2934	-5000	5000	
	1.11g	1992	0	1000	
	1.11h	2133	1000	2000	
	1.11i	3534	3000	3000	
			23199		

<sup>a</sup>Relative to time of fault nucleation as indicated by reversal of slope in stress- displacement plot. This time would correspond to the onset of tertiary creep in a constant-stress experiment.

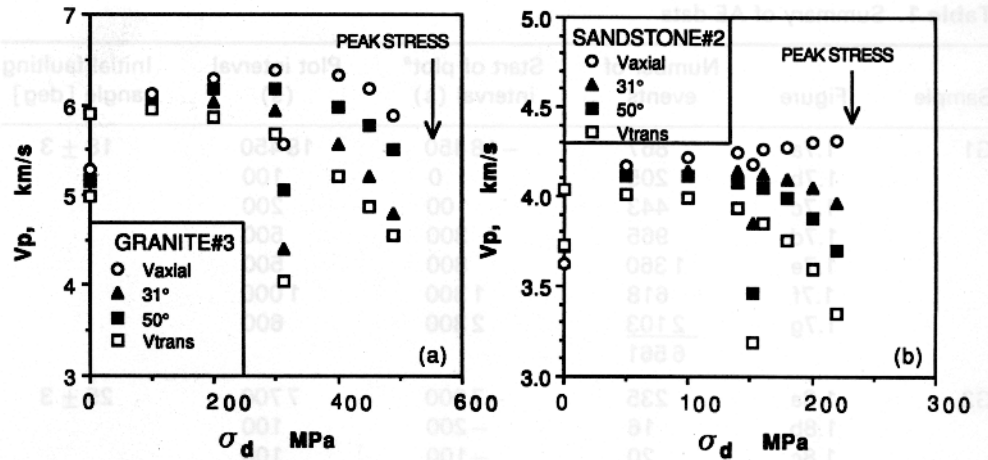


**Figure 6.** Average  $P$ -wave velocity structure used in hypocentral inversion routine for (a) sample G3 and (b) sample S2 throughout loading histories. Solid symbols represent measured velocities; open symbols represent calculated fast- and slow-direction velocities.

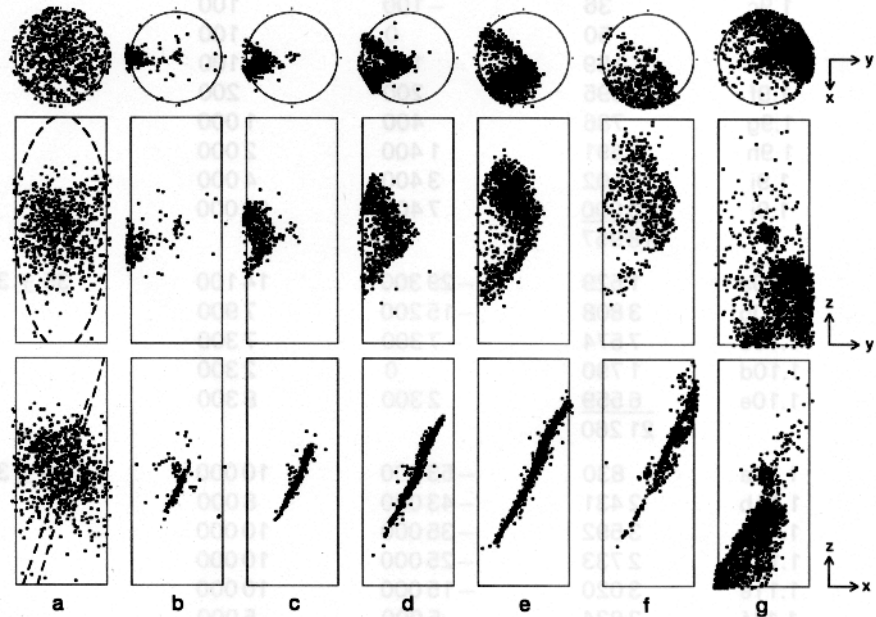


**Figure 7.** Plots of AE locations for sample G1. Bottom plot of each set is view looking along-strike of eventual fracture plane. Middle plot is face-on view of fault in which sample has been rotated counterclockwise  $90^\circ$ . Top plot is view looking down on sample. Projections of surface trace of eventual fault plane are shown in (a) for reference. Each point represents one AE event. Associated statistics are given in Table 1. Stress intervals for each plot are indicated in Figures 3a and 5a. Fault nucleation occurs in plot (b).

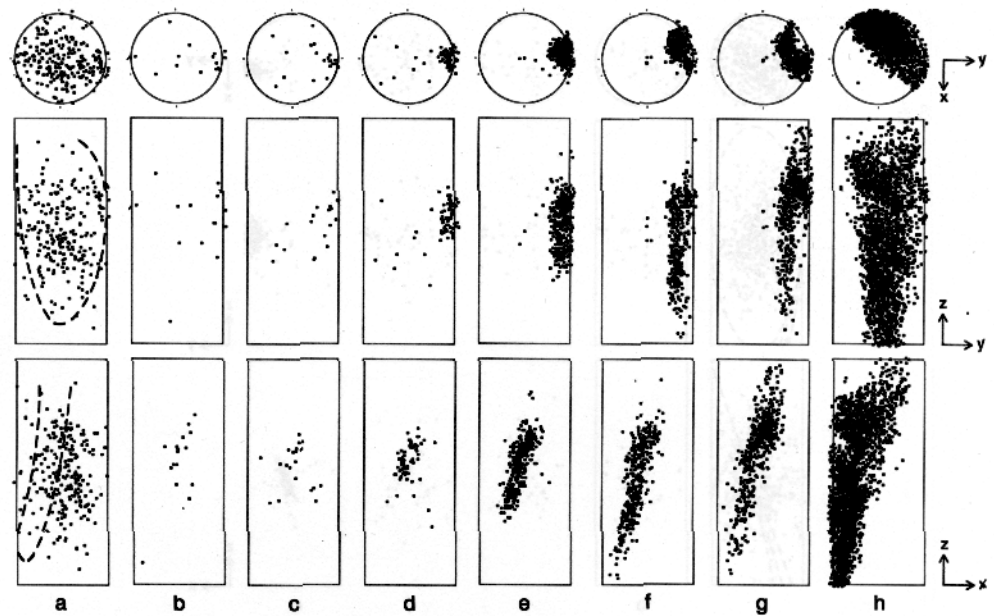


**Figure 8.** Plots of AE locations for sample G2 (explanation is similar to that for Figure 7). Stress intervals for each plot are indicated in Figure 3b. Fault nucleation occurs in plot (d). Owing to equipment problems, this experiment gave the least accurate locations.

experiment. The acoustic emission pattern shifts dramatically in Figure 7b in which AE events that occurred during the 100 s following fault nucleation are plotted. While a few events are still occurring throughout the volume of the sample, most events are now clustered near the surface of the sample in the nucleation zone. In the next 200 s (Figure 7c), distributed AE events have all but ceased and a distinct fracture front, or process zone, has developed that is growing out from the nucleation site. The fracture tends to grow upward and across the sample more easily than downward (Figure 7d,e,f), possibly reflecting the fact that it has started to graze the bottom endplug. A segment of data was lost following Figure 7f while we measured acoustic velocity in the sample (shown as shallow-sloping ramp in Figure 3a). The final AE events recorded (Figure 7g) show growth of the lower right corner of the fault plane, as well as numerous events off the fault due to the interference with the endplug. While the AE locations in the central region of the sample coincide with the observed fault plane, events near the ends of the sample show a systematic bias away from the observed fault. As discussed in the previous section, we attribute this discrepancy to errors in the velocity structure supplied to the inversion program. A 5% adjustment in the velocity structure will rotate the locus of AE events to agree with the observed fault surface. We are currently exploring ways of improving our velocity determinations to correct this problem.

Acoustic emission locations from experiment G2 are plotted in Figure 8 and referenced to the stress history in Figure 3b. A relatively complicated, steeply dipping fault formed in this experiment (seen from fault trace in Figure 8a). Similarly to experiment G1, events occurring through peak stress (Figure 8a,b) were distributed throughout the central region of the sample. However, AE activity in this case shifted to the fault nucleation region over an approximately 100s interval (Figure 8c). Owing to equipment

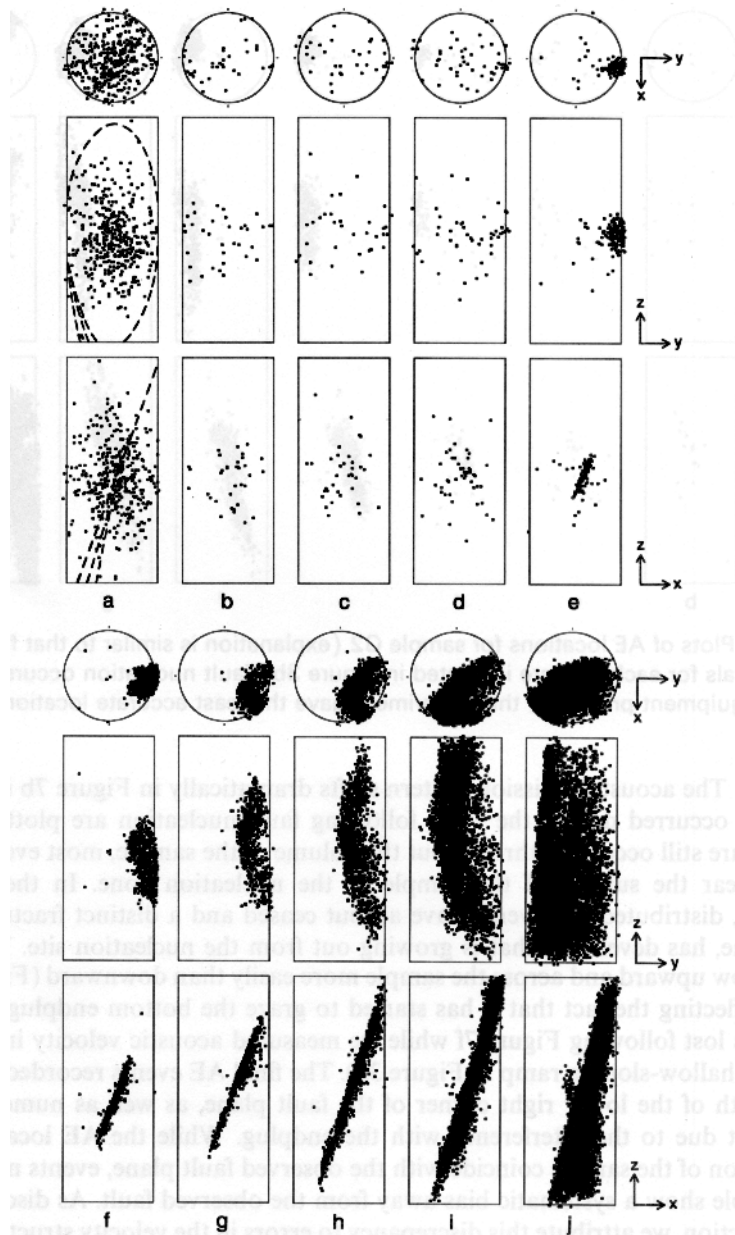


**Figure 9.** Plots of AE locations for sample G3 (explanation is similar to that for Figure 7). Stress intervals for each plot are indicated in Figures 3c and 5b. Fault nucleation occurs in plot (d).

problems, event locations are not as accurate in this experiment as in the other granite runs, although the fault plane is again seen to nucleate at the sample surface near the sample mid-plane (Figure 8d). The fault then grows away from the nucleation site across the sample (Figures 8e-h).

AE locations from experiment G3 are plotted in Figure 9, with stress history shown

in Figures 3c and 5b. Experiment G3 was the last run of the series and, from the travel-time residuals (shown in the appendix), appears to have the most accurate locations of all the runs. The final fault surface (indicated in Figure 9a) again intersected one endplug, causing distributed damage to the bottom end of the sample during the late stages of faulting. As in the other granite runs, loading through peak stress produced distributed microcracking in the central region of the sample (Figure 9a,b). In the 100 s prior to nucleation (Figure 9c), there is a suggestion of increased AE activity in the nucleation zone, although this clustering becomes more organized in the next 100 s (Figure 9d). In the next 200 s (Figure 9e) the nascent fault plane has clearly formed, again on the sample surface near the mid-plane. In the remainder of the plots, the fault plane propagates across the sample, eventually bisecting it. During the late stages of fault growth, the fault tends to steepen. This feature was observed in all three granite experiments where the initial fault formed at an angle of 18-25° to the sample axis (Table 1) but the trace where the fault broke out on the opposite surface of the sample was consistently steeper, forming angles of 5-15°.

### 3.2. Fault formation in sandstone

A number of features of the sandstone experiments differed from the granite runs. Peak stress, and therefore stress drop, was lower for the sandstone. The overall weakening of the granite samples during fault formation was 400-420 MPa, whereas for the sandstone, the drop in differential stress during faulting was 70-80 MPa. Inclination of fractures in the sandstone was approximately 32° as compared to 18-25° for the granite. In addition, the acoustic emissions that occurred during deformation were different for the two rock types. Little AE occurred in the granite samples below about 60% of peak stress, while in the sandstone samples significant AE was occurring by 30 to 40% peak stress. The overall AE activity was also more intense in the sandstone samples than in granite. We interpret the enhanced sandstone activity as the result of distributed grain crushing and sliding. The open pore structure in the Berea (18% porosity) results in stress concentrations at the grain contacts, making this rock susceptible to grain crushing and grain rearrangement when loaded.

The progression of faulting in the sandstone was also notably different from that in the granite. AE locations from sample S1 are shown in Figure 10 and can be compared to the stress history plotted in Figure 4a. A region of intense AE activity occurred in sample S1, beginning with the initial loading (Figure 10a). This activity was primarily in the core of the sample and was located on the eventual fracture plane. Owing to the contrast in modulus between the sandstone and the steel endplugs, conically-shaped zones of high shear stress develop at the ends of samples loaded in this configuration. The coincidence of early AE activity, shown in Figures 10a and 10b, with the zone of high shear stress may indicate that these features are related. In any case, by peak stress (Figure 10b) the region of intense activity has broadened and considerable uniform microcracking has been generated throughout the rest of the sample. For the next 7000 s (Figure 10c), the stress steadily drops by 10 MPa, indicating that the damage zone is gradually weakening the sample, and the stress must be decreased slightly to maintain constant AE rate. During this period, AE activity also migrates to the periphery of the damage zone (outward and downward). In some sense, the nucleation stage of the fracture has been completed by Figure 10d. While this process is not as distinct as in the granite samples, a change in the character of the AE event locations occurs between

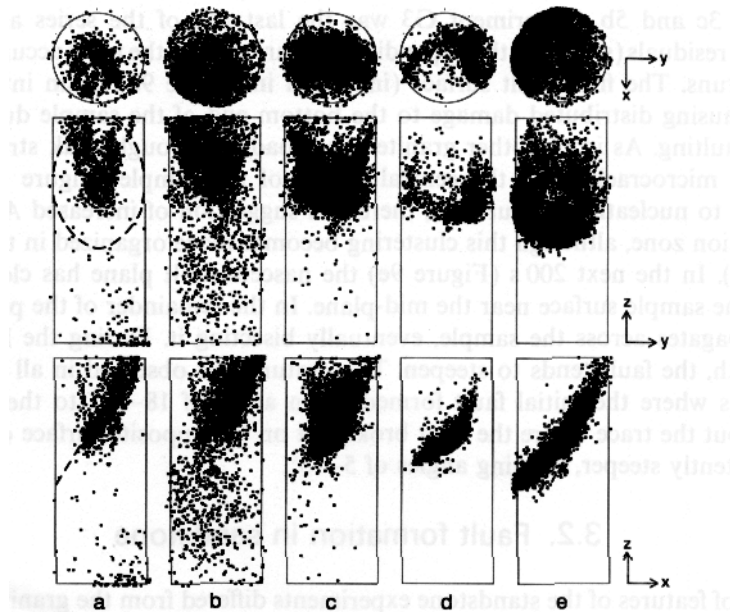


**Figure 10.** Plots of AE locations for sample S1 (explanation is similar to that for Figure 7). Stress intervals for each plot are indicated in Figure 4a. Unlike granite experiments, AE activity concentrated in region of fault from beginning of experiment; possibly indicating a flaw in sample. AE activity appears to organize into planar feature in (d). In one sense, this interval represents fault nucleation.

Figures 10c and 10d. In the along-strike views (bottom plots), the AE events become notably localized along the eventual fracture plane by Figure 10d. In the face-on views (middle plots), a narrow fracture front has developed by Figure 10d with most activity concentrated on the right-hand side of the fracture as it propagates out to the sample surface. This process continues in Figure 10e, where the toe and lower left side of the fault are formed. A more detailed view of the events shown in Figures 10d and 10e reveals that after the fracture breaks through to the surface on the right side of the sample, the fracture front systematically progresses down, around the toe and up the left side.

AE locations from sandstone sample S2 are shown in Figure 11 and can be compared to the stress history plotted in Figures 4b and 5c. The surface trace of the eventual fracture plane is indicated in Figure 11a. Also shown in Figure 11a are AE locations for events occurring during loading to 73% peak stress. In this case, two and possibly three clusters of microcracking occur during the early stages of loading. The most distinct cluster, in the central region of the sample, occurs on the eventual fault plane and within 10 mm of the sample surface. This cluster appears to be the nucleation site for the fracture plane. Visual inspection of the sample after the experiment showed nothing unusual about this area. The upper cluster of activity occurs in the core of the sample in the region of high shear stress discussed in the previous paragraph. Loading to peak stress (Figure 11b) results in continued AE activity in these same regions, although the activity at this stage is diffuse, extending over volumes with diameters of approximately 40 mm. Over the next 5.5 hours (Figures 11 c, d), AE activity gradually shifts to the fault

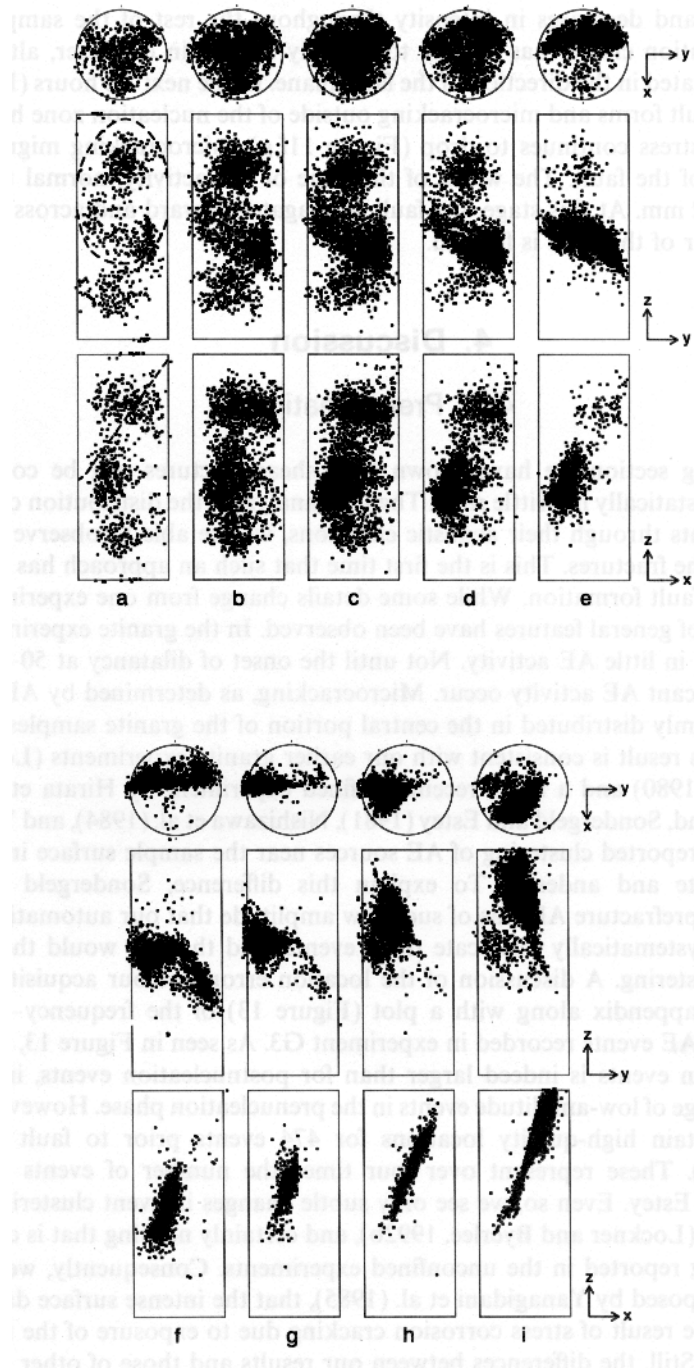


**Figure 11.** Plots of AE locations for sample S2 (explanation is similar to that for Figure 7). Stress intervals for each plot are indicated in Figures 4b and 5c. Similarly to sample S1, AE activity is localized in early loading stage of experiment, suggesting strength inhomogeneity in this sample. AE activity does not become well organized into planar feature until plots (e) and (f), which are well beyond peak strength.

nucleation site and decreases in intensity throughout the rest of the sample. By this stage the nucleation cluster has shrunk to roughly 30 mm in diameter, although it is somewhat elongated in the direction of the fault plane. In the next 2.8 hours (Figure 11e), the toe of the fault forms and microcracking outside of the nucleation zone has virtually ceased. As the stress continues to drop (Figure 11f, g), microcracking migrates to the lower left side of the fault. The width of the zone of AE activity, normal to the fault plane, is now 12 mm. At this stage, the fault propagates upward and across the sample as the remainder of the fault is formed.

## 4. Discussion

### 4.1. Prenucleation

In the preceding section we have shown how shear fractures can be controlled to propagate quasistatically in brittle rock. Then, by analyzing the distribution of impulsive microcrack events through their acoustic emissions, we are able to observe nucleation and growth of the fractures. This is the first time that such an approach has been taken to the study of fault formation. While some details change from one experiment to the next, a number of general features have been observed. In the granite experiments, early loading resulted in little AE activity. Not until the onset of dilatancy at 50-60% peak stress did significant AE activity occur. Microcracking, as determined by AE locations, remained uniformly distributed in the central portion of the granite samples until after peak stress. This result is consistent with our earlier granite experiments (Lockner and Byerlee, 1977a, 1980) and a more recent confined experiment by Hirata et al. (1987). On the other hand, Sondergeld and Estey (1981), Nishizawa et al. (1984), and Yanagidani et al. (1985) all reported clustering of AE sources near the sample surface in uniaxially deformed granite and andesite. To explain this difference, Sondergeld and Estey speculated that prefracture AE was of such low amplitude that our automatic detection system would systematically mislocate these events, and that we would therefore not detect event clustering. A discussion of the location errors for our acquisition system appears in the appendix along with a plot (Figure 13) of the frequency-magnitude distribution for AE events recorded in experiment G3. As seen in Figure 13, the  $b$ -value for prenucleation events is indeed larger than for postnucleation events, indicating a greater percentage of low-amplitude events in the prenucleation phase. However, we were still able to obtain high-quality locations for 474 events prior to fault nucleation (Figures 9a,b,c). These represent over four times the number of events located by Sondergeld and Estey. Even so, we see only subtle changes in event clustering prior to fault nucleation (Lockner and Byerlee, 1992b), and certainly nothing that is comparable to the clustering reported in the unconfined experiments. Consequently, we prefer the explanation proposed by Yanagidani et al. (1985), that the intense surface damage they observed was the result of stress corrosion cracking due to exposure of the free surface to water vapor. Still, the differences between our results and those of other researchers must be considered an open question and further study of this problem is required.

Related to this issue, a sampling problem that is inherent to AE studies should be kept in mind. While numerous studies have pointed out the close correlation between number of AE events and inelastic strain in the sample (e.g. Lockner and Byerlee, 1977c, 1980), the number of new microcracks detected by AE is a small fraction of the total

microcrack population. As we show in the appendix, this condition holds for AE studies in general. As an example, we consider the AE detected during the initial loading stages in our granite experiments. During this period, 2000-5000 AE events were typically detected. For a grain size in Westerly granite of  $\sim 0.3$  mm, this gives approximately one AE event for every 3000 to 8000 grains, or one AE event per  $200 \text{ mm}^3$ . We can make a rough comparison between AE event density and microcrack density in the following way. Madden (1984) analyzed crack data compiled by Hadley (1975) for deformation of Westerly granite. Hadley reported that the largest cracks showing significant increase in crack density during loading were 30-100  $\mu\text{m}$  long, a result that we have independently confirmed (Lockner et al., 1992). She found that by peak stress, the areal density of these cracks had increased by  $115 \text{ cracks/mm}^2$ . Assuming that crack length and width were approximately the same, volumetric crack density of this size crack had increased during loading on the order of  $3000 \text{ cracks/mm}^3$ . Thus, cracking events detected by AE represent a small fraction of the total microcrack damage occurring in the rock. How representative the microcracks detected by AE are of the overall microcrack population is still unknown. For fracture studies, however, AE activity does appear to be a reliable indicator of zones of fault movement and crack damage. The excellent agreement between AE locations and observed faults in this study as well as faults and hydrofracture surfaces in Lockner and Byerlee (1977b) and Lockner et al. (1982) supports this conclusion.

#### 4.2. Fault nucleation

The observation that in our granite experiments the fault consistently nucleated at the sample surface suggests that nucleation is controlled by conditions at the sample boundaries in the triaxial geometry. It is possible that a misalignment of the loading frame caused bending of the sample and a high-stress region on the surface. However, if this were the case, we would expect to see increased AE activity from this region during the entire loading cycle. Figures 7-9 show that this was not the case. An alternate explanation is based on the observation that fracture nucleation in brittle rock involves microcracking and the development of a dilatant zone. Since damaging earthquakes nucleate at depth in the earth, the dilating nucleation zone must expand against the surrounding rock mass. This surrounding rock acts to confine and support the dilatant zone. In the triaxial test geometry, however, the confining fluid has zero modulus (control system maintains constant pressure regardless of volume change). Thus, while a failing region on the rock surface will do work as it expands against the confining fluid, there will be no net transfer of stress as would be the case for a dilating zone in the interior of the sample. As a result, we would always expect the fault to nucleate at the rock surface. This interpretation is supported by bifurcation analysis of finite-sized samples in which failure also tends to occur on the sample surface. In this sense, triaxial rock tests provide a lower bound for the strength of rock deformed under more appropriate boundary conditions. We are currently considering methods of fabricating composite samples that will provide boundary conditions more appropriate for earthquake nucleation studies. Fault nucleation appeared to occur in the interior of at least the first sandstone experiment. However, it should be noted that the dilatancy needed for fault formation in a low-porosity granite is only a few percent. Berea sandstone contains about 18% porosity and also has a lower modulus than granite. As a result there should be room for grains to readjust locally with little transfer of load to the surrounding material.

In contrast to the granite experiments, AE localization occurred during the early stages of loading in both sandstone experiments. Berea is a bedded sandstone and consequently exhibits strength anisotropy. From the early localization of AE events in the sandstone experiments, we infer that Berea also has significant strength heterogeneity. This heterogeneity appears to be of sufficient magnitude to dictate where failure will initiate. One interesting feature of the sandstone experiments is that early AE clustering was relatively diffuse, filling volumes of 40 mm or more in linear dimension. Then, as the fracture surface formed, the zone of microcracking narrowed in the direction perpendicular to the fault to between 10 and 20 mm thickness. For comparison, the zone of crushed material that defined the surface trace of the fracture was less than 2 mm thick.

In the granite experiments, fault nucleation involved the occurrence of a relatively small number of large-amplitude events. This can best be seen in Figure 9d where about 10 events have occurred in the nucleation zone. With the addition of about 20 more events (included in Figure 9e), the nucleation patch that initially had no preferred orientation has established the narrow diagonal structure which defines the orientation of the final fault plane. In the granite samples, the nucleation zone appears to require a volume of approximately  $2 \text{ cm}^3$ . In the sandstone samples the nucleation zone, just before fault propagation, is approximately  $9 \text{ cm}^3$ . As defined by the AE locations, the nascent fault plane that forms in the granite samples has a half-disk shape (Figures 7b, 9e), with a thickness of no more than 3 mm and radius of approximately 15 mm. From this initial structure, the fault grows in-plane away from the nucleation site.

#### 4.3. Fault growth

Once fault nucleation begins in the granite samples, it proceeds relatively quickly to establish the nascent fault plane. Following this phase of fault development is the growth phase, in which a band of AE activity develops, indicating a zone of intense microcracking, and propagates away from the nucleation site. Thus we are able to observe mixed modes II and III shear propagation as the fault grows across the sample. Growth in the direction perpendicular to the sample axis is pure mode III anti-plane shear while propagation towards the sample ends is nearly pure mode II in-plane shear. A relatively quiet region forms behind the advancing fracture front (Figures 12, 7c-e, 9g-i), indicating that intense grain crushing is restricted to the fracture front. Sliding must continue on the fault surface after the fracture front passes, furthering the process of grain comminution. However, the relatively few large-amplitude AE events in this region suggest that most large grains have been crushed during the passage of the fracture front. The localized zone of grain crushing at the tip of the advancing fault corresponds closely to the process zone discussed, for example, in the Rice (1980, 1984) model for shear crack propagation along an existing fault. In this model the process zone, having in-plane dimension  $w$ , is the region at the crack tip over which the shear stress drops from the peak value to the frictional strength level. If we assume that the breakdown zone is represented by the region of intense AE activity, samples G1 and G3 give  $w_{\text{granite}} \approx 20\text{-}50 \text{ mm}$  (Figures 7, 9, and 12). Wong (1982a) reported estimates of  $w$  for room temperature experiments that ranged from 40 to 290 mm. Thus our estimates of  $w$  fall near the lower end of the range tabulated by Wong. In the sandstone samples, the breakdown zone that developed was never as well-defined as in the granite experiments. An approximate value of  $w$ , based on the AE patterns, is  $w_{\text{sandstone}} \approx 60\text{-}90 \text{ mm}$ .

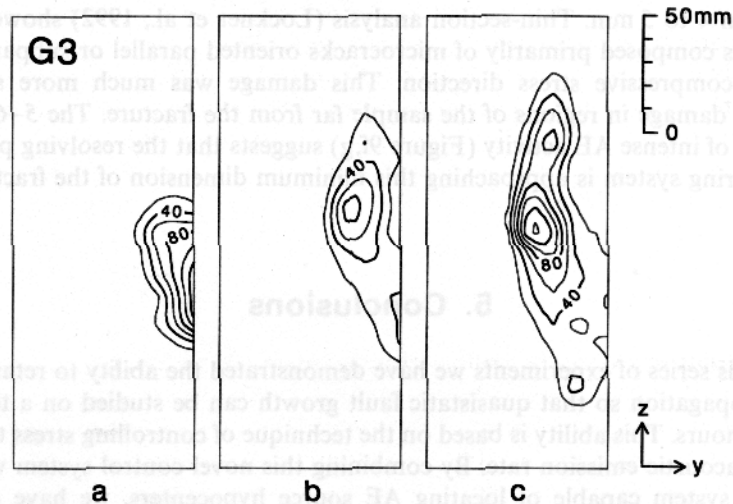


**Figure 12.** Density of AE events during progressive time intervals in Experiment G3. Fault plane is viewed face-on. Time intervals correspond to Figure 9f, g, and h. Contour interval is 20 events/cm<sup>2</sup>. Width  $w$  of process zone is taken to correspond to width of band of AE activity.

The shear fracture energy, or energy release rate,  $\mathcal{G}$  is a fundamental quantity used in models of shear fracture propagation.  $\mathcal{G}$  represents the energy flux needed to extend the fracture. Following Rice (1980), Wong (1982a) compiled representative values of  $\mathcal{G}$  from confined laboratory experiments. Values ranged from  $0.3 \times 10^4$  to  $7.3 \times 10^4$  J m<sup>-2</sup> for granite and quartzite. The procedure for calculating  $\mathcal{G}$  assumes that the sample is small enough so that the entire fault plane slides as a unit. While this is not the case for our experiments, we can still provide a rough estimate of  $\mathcal{G}$ . Sample G1 yields a value of  $\mathcal{G}_{\text{granite}} = 1.3 \times 10^4$  J m<sup>-2</sup> and sample S2 yields  $\mathcal{G}_{\text{sandstone}} = 0.25 \times 10^4$  J m<sup>-2</sup>, in good agreement with the earlier reported values. In a related paper (Lockner et al., 1991) we use the radiated acoustic energy to map the local energy release rate on the fault, much as seismic moment is used to infer stress drop heterogeneity for large earthquakes. The rapid drop in stress level that marks the transition from fault initiation to fault propagation indicates that it is easier for a fault to grow once its initial structure has formed. It may therefore be inappropriate to infer properties of the growth of fractures from experiments on small samples in which nucleation dominates. We intend to explore this possibility in future experiments.

The thickness,  $h$ , of the fracture normal to its plane is another important parameter for describing faults. Fracture energy for aggregates is generally significantly greater than for single crystals. The main reason for this increase is the development of a zone of damage that moves with the advancing fault tip. The development of this damage zone depends on mobilization of preexisting flaws which are abundant in multigrain aggregates. By impregnating fractured samples with dyed epoxy, the damaged region bordering the fault can easily be measured. In sample G2, the fault propagated toward the upper endplug and stopped about 25 mm from it (Figure 8). The damage zone at the arrested crack tip was  $h = 1.0 \pm 0.2$  mm. Near the lower part of the fracture, where possibly 0.5 mm shear slip had occurred, damage zone thickness was approximately 1.5-3 mm. In sample G3, where more slip occurred ( $\sim 1$  mm), damage zone thickness

ranged from 4 to 5 mm. Thin-section analysis (Lockner et al., 1992) showed that this damage was composed primarily of microcracks oriented parallel or subparallel to the maximum compressive stress direction. This damage was much more severe than microcrack damage in regions of the sample far from the fracture. The 5-6 mm width of the zone of intense AE activity (Figure 9f,g) suggests that the resolving power of the AE monitoring system is approaching this minimum dimension of the fractures.

## 5. Conclusions

Through this series of experiments we have demonstrated the ability to retard unstable fracture propagation so that quasistatic fault growth can be studied on a timescale of minutes to hours. This ability is based on the technique of controlling stress to maintain a constant acoustic emission rate. By combining this novel control system with an AE acquisition system capable of locating AE source hypocenters, we have observed a number of features of fracture formation. The brittle fracture process, under triaxial conditions, was found to involve three stages:

(1) *Distributed damage during loading of the sample to peak stress.* In granite samples, dilatancy and the associated microcracking were found to be distributed uniformly throughout the sample. No clustering of AE locations was observed that was comparable to clustering reported in previous unconfined experiments. In sandstone, however, AE clustering was observed from the earliest stages of loading in regions which ultimately developed into the fault plane. This clustering was initially diffuse but became more localized as the sample was loaded. It is interpreted as indicating the presence of significant weak zones or zones of stress concentration which acted as nucleation sites and determined the location of the fault plane.

(2) *Fault nucleation.* In granite, soon after peak stress, a zone of intense AE activity formed on the surface, near the sample mid-plane. The nucleation site, with volume approximately  $2 \text{ cm}^3$ , rapidly evolved into the nascent fault, narrowing into a half-disk shape that defined the position and orientation of the fracture. This nucleation process was accompanied by a rapid drop in stress. In the sandstone samples, this nucleation stage involved localization of the relatively diffuse AE activity into a roughly planar feature.

(3) *Fault propagation.* In both granite and sandstone samples, the newly formed fault grew by developing a characteristic zone of intense AE activity which is interpreted as a fracture front propagating across the sample. This process zone was 10-50 mm wide in granite and 60-90 mm wide in sandstone. The thickness of the process zone, normal to the fracture surface, was 1-5 mm in granite and approximately 10 mm in sandstone.

These results suggest interesting new avenues of research for earthquake studies. The nucleation patch, size for the highly homogeneous Westerly granite was only a few cubic centimeters. Once the fault nucleated on this size scale, further growth in a compliant system such as the earth would be rapid and uncontrolled. Such a small nucleation zone would be very difficult to recognize remotely. On the other hand, the sandstone samples showed that a heterogeneous material would generate zones of intense activity well before catastrophic failure. The nucleation process in this case involved a concentration of this acoustic activity into a more and more compact region, as well as a gradual evolution towards a planar shape. Thus, if the heterogeneity that controls

fault nucleation in the earth is on a large enough scale, the possibility exists that the occurrence and evolution of the nucleation zone could be identified remotely.

## Acknowledgements

Many people have contributed to the success of these experiments. In particular, we thank T. Madden, Z. Reches, J. Rudnicki, T. Satoh, J. Savage and T.-f. Wong for their thoughtful and constructive comments.

## References

- Byerlee, J.D. and Lockner, D.A. (1977). Acoustic emission during fluid injection in rock. In *Proc. 1st Conf. on Acoustic Emission/Microseismic Activity in Geological Structures and Materials* (ed. H.R. Hardy and F.W. Leighton), pp. 87-98. Trans-Tech. Publications, Clausthal-Zellerfeld.
- Costin, L.S. (1987). Deformation and failure. In *Fracture Mechanics of Rock* (ed. B.K. Atkinson), pp. 167-215. Academic Press, New York.
- Du, Y. and Aydin, A. (1991). Interaction of multiple cracks and formation of echelon crack arrays. *Int. J. Numerical and Analytical Methods in Geomech.* **15**, 205-218.
- Fraser-Smith, A.C., Bernardi, A., McGill, P.R., Ladd, M.E., Helliwell, R.A., and Villard, O.G., Jr. (1990). Low-frequency magnetic field measurements near the epicentre of the Ms 7.1 Loma Prieta earthquake. *Geophys. Res. Lett.* **17**, 1465-1468.
- Gutenberg, B. and Richter, C.F. (1949). *Seismicity of the Earth*. Princeton University Press.
- Hadley, K. (1975). Dilatancy: further studies in crystalline rocks. Ph.D. thesis, MIT, Cambridge, Mass.
- Hallbauer, D.K., Wagner, H., and Cook, N.G.W. (1973). Some observations concerning the microscopic and mechanical behavior of quartzite specimens in stiff, triaxial compression tests. *Int. J. Rock Mech. Min. Sci.* **10**, 713-726.
- Hirata, T., Satoh, T., and Ito, K. (1987). Fractal structure of spatial distribution of microfracturing in rock. *Geophys. J. R. Astron. Soc.* **90**, 369-374.
- Horii, H. and Nemat-Nasser, S. (1985). Compression-induced microcrack growth in brittle solids: axial splitting and shear failure. *J. Geophys. Res.* **90**, 3105-3125.
- House, L.S., Kranz, R.L., Nishizawa, O., and Satoh, T. (1989). Use of acoustic emissions to investigate stresses in laboratory rock samples. *EOS (Trans. Amer. Geophys. Union)*, **70**, 1340.
- Jaeger, J.C. and Cook, N.G.W. (1984) *Fundamentals of Rock Mechanics*. Chapman and Hall, New York.
- Johnston, M.J.S. (1990). Review of continuous high precision borehole strain measurements near the locked and creeping sections of the San Andreas fault. *Abst. of NSF-USGS Workshop on Crustal Deformation Measurement and Earthquake Mechanics, Morro Bay, California, March 18, 1990*.
- Johnston, M.J.S., Linde, A.T., Gladwin, M.T., and Borchardt, R.D. (1987). Fault failure with moderate earthquakes. *Tectonophysics* **144**, 189-206.
- Lawn, B.R. and Wilshaw, T.R. (1975). *Fracture of Brittle Solids*. Cambridge University Press.
- Linde, A.T. and Johnston, M.J.S. (1989). Source parameters of the October 1, 1987 Whittier Narrows earthquake from crustal deformation data. *J. Geophys. Res.* **94**, 9633-9643.
- Lockner, D.A. and Byerlee, J.D. (1977a). Acoustic emission and fault formation in rocks. In *Proc. 1st Conf. on Acoustic Emission/Microseismic Activity in Geol. Structures and Materials* (ed. H.R. Hardy and F.W. Leighton), pp. 99-107. Trans-Tech. Publications, Clausthal-Zellerfeld.
- Lockner, D.A. and Byerlee, J.D. (1977b). Hydrofracture in Weber sandstone at high confining pressure and differential stress. *J. Geophys. Res.* **82**, 2018-2026.

- Lockner, D.A. and Byerlee, J.D. (1977c). Acoustic emission and creep in rock at high confining pressure and differential stress. *Bull. Seismol. Soc. Am.* **67**, 247-258.
- Lockner, D.A. and Byerlee, J.D. (1978). Velocity anomalies: an alternative explanation based on data from laboratory experiments. *Pure Appl. Geophys.* **116**, 765-772.
- Lockner, D.A. and Byerlee, J.D. (1980). Development of fracture planes during creep in granite. In *2nd Conf. on Acoustic Emission/Microseismic Activity in Geological Structures and Materials* (ed. H.R. Hardy and F.W. Leighton), pp. 11-25. Trans-Tech. Publications. Clausthal-Zellerfeld.
- Lockner, D.A. and Byerlee, J.D. (1992a). Fault growth and acoustic emissions in confined granite. *Appl. Mechanics Rev.* (in press).
- Lockner, D.A. and Byerlee, J.D. (1992b). Precursory AE patterns leading to rock fracture. In *Proc. 5th Conf. on Acoustic Emission/ Microseismic Activity in Geol. Structures and Materials* (ed. H.R. Hardy), 14 pp. Trans-Tech. Publications, Clausthal-Zellerfeld, Germany (in press).
- Lockner, D.A. and Madden, T.R. (1991a). A multiple crack model of brittle fracture part I: non-time-dependent simulations. *J. Geophys. Res.* **96**, 19623-19642.
- Lockner, D.A. and Madden, T.R. (1991b). A multiple crack model of brittle fracture part II: time-dependent simulations. *J. Geophys. Res.* **96**, 19643-19654.
- Lockner, D.A., Recher, Z., and Moore, D.E. (1992). Microcrack interaction leading to shear fracture. In *Proc. 33rd U.S. Symposium on Rock Mechanics* (ed. W. Wawersik), A.A. Balkema, Rotterdam.
- Lockner, D.A., Walsh, J.B., and Byerlee, J.D. (1977). Changes in seismic velocity and attenuation during deformation of granite. *J. Geophys. Res.* **82**, 5374-5378.
- Lockner, D.A., Summers, R., Moore, D., and Byerlee, J.D. (1982). Laboratory measurements of reservoir rock from the Geysers geothermal field, California. *Int. J. Rock Mech. Min. Sci. & Geomech. Abstr.* **19**, 65-80.
- Lockner, D.A., Byerlee, J.D., Kuksenko, V., Ponomarev, A., and Sidorin, A. (1991). Quasi-static fault growth and shear fracture energy in granite. *Nature* **350**, 39-42.
- Madden, T.R. (1983). Microcrack connectivity in rocks: a renormalization group approach to the critical phenomena of conduction and failure in crystalline rocks. *J. Geophys. Res.* **88**, 585-592.
- Nishizawa, O., Onai, K., and Kusunose, K. (1984). Hypocenter distribution and focal mechanism of AE events during two stress stage creep in Yugawara andesite. *Pure Appl. Geophys.* **122**, 36-52.
- Recher, Z. and Lockner, D. (1990). Self-organized cracking - a mechanism for brittle faulting. *EOS, Amer. Geophys. Union Trans.* **71**, 1586.
- Rice, J.R. (1980). The mechanics of earthquake rupture. In *Physics of the Earth's Interior* (Proc. Int'l School of Physics "E. Fermi", course 78, 1979) (eds. A.M. Dziewonski and E. Boschi). Italian Physical Society/North Holland.
- Rice, J.R. (1984). Shear instability in relation to the constitutive description of fault slip. In *Proc. 1st Int. Congress on Rockbursts and Seismicity in Mines*, pp. 57-62. SAIMM, Johannesburg.
- Sammis, C.G. and Ashby, M.F. (1986). The failure of brittle porous solids under compressive stress states. *Acta Metall.* **34**, 511-526.
- Scholz, C.H. (1968). Experimental study of the fracturing process in brittle rocks. *J. Geophys. Res.* **73**, 1447-1454.
- Sondergeld, C.H. and Estey, L.H. (1981). Acoustic emission study of microfracturing during the cyclic loading of Westerly granite. *J. Geophys. Res.* **86**, 2915-2924.
- Spetzler, H., Sobolev, G., Sondergeld, C., Salov, B., Getting, I., and Koltsov, A. (1981). Surface deformation, crack formation, and acoustic velocity changes in pyrophyllite under polyaxial loading. *J. Geophys. Res.* **86**, 1070-1080.
- Tapponnier, P. and Brace, W.F. (1976). Development of stress-induced microcracks in Westerly granite. *Int. J. Rock Mech. Min. Sci.* **13**, 103-112.
- Terada, M., Yanagidani, T., and Ehara, S. (1984). A. E. rate controlled compression test of rocks. In *3rd Con on Acoustic Emission/Microseismic Activity in Geological Structures and Materials* (ed. H.R. Hardy and F.W. Leighton), pp. 159-171. Trans-Tech. Publications, Clausthal-Zellerfeld.

- Wawersik, W.R. (1973). Time-dependent behavior of rock in uniaxial compression. In *Proc. 14th Symposium on Rock Mechanics*, pp. 85-106.
- Wawersik, W.R. and Brace, W.F. (1971). Post-failure behavior of a granite and a diabase. *Rock Mech.* **3**, 61-85.
- Wawersik, W.R. and Fairhurst, C. (1970). A study of brittle rock fracture in laboratory compression experiments. *Int. J. Rock Mech. Min. Sci.* **7**, 561-575.
- Weeks, J.D., Lockner, D.A., and Byerlee, J.D. (1978). Change in  $b$ -values during movement on cut surfaces in granite. *Bull. Seismol. Soc. Am.* **68**, 333-341.
- Wong, T.-f. (1982a). Shear fracture energy of Westerly granite from post-failure behavior. *J. Geophys. Res.* **87**, 990-1000.
- Wong, T.-f. (1982b). Effects of temperature and pressure on failure and post-failure behavior of Westerly granite. *Mechanics of Materials* **1**, 3-17.
- Yanagidani, T., Ehara, S., Nishizawa, O., Kusunose, K., and Terada, M. (1985). Localization of dilatancy in Ohshima granite under constant uniaxial stress. *J. Geophys. Res.* **90**, 6840-6858.

## Appendix Evaluation of Location Accuracy

In this appendix we examine the resolving power of the AE acquisition system used in these experiments. Lockner and Byerlee (1978) demonstrated the susceptibility of an automatic arrival-time detector (or P-picker in seismological parlance) to systematically picking arrivals of small-amplitude, emergent signals too late. It is necessary, therefore, to consider the effect of this sampling bias on the location accuracy of the hypocentral inversion routine. This is an important issue, since the conclusions of our current experiments rely on our ability to locate accurately AE sources. In previous studies (Lockner and Byerlee, 1977b, 1980; Lockner et al., 1982) direct correspondence between AE locations and observed fault planes has demonstrated our ability to locate faults through inversion of AE arrival times. We now present a more quantitative assessment of our location accuracy.

A useful starting point in a discussion of location bias is through the use of an amplitude–frequency plot. Weeks et al. (1978) and Lockner et al. (1991) have shown that, as with earthquakes, AE events obey the well-known frequency-magnitude relation

$$N(M) = a - bM$$

(Gutenberg and Richter, 1949) where  $N$  is the number of earthquakes greater than magnitude  $M$  and  $a$  and  $b$  are constants. Using the complete data set obtained from experiment G3 as well as the subset of prenucleation events, we have plotted cumulative number of events as a function of  $\log(\text{amplitude})$  in Figure 13. In this plot, amplitudes have been adjusted for attenuation due to geometric spreading and are shown as the amplitude that would be expected 10 mm from the hypocenter. If we define the RMS travel time residual as  $TT^{\text{rms}} = \sqrt{(\mathbf{R}^T \cdot \mathbf{R}/6)}$ , we can set an arbitrary cutoff for potentially ‘successful’ event locations of  $TT^{\text{rms}} < 5 \mu\text{s}$ . On this criterion, the total number of events successfully located in this experiment was 45 713. Plotted in the upper left corner is the total number of events (165 117) that triggered the acquisition system at the preset threshold level. As seen in this plot, most AE events have small amplitudes. For example, we could have doubled the number of recorded events simply by lowering the threshold level by 30%. This fact, resulting from the nature of the frequency–magnitude relation, can be expected for any brittle rock deformation experiment. Of the events that did trigger the system, some 28% gave acceptable locations according to this initial criterion.

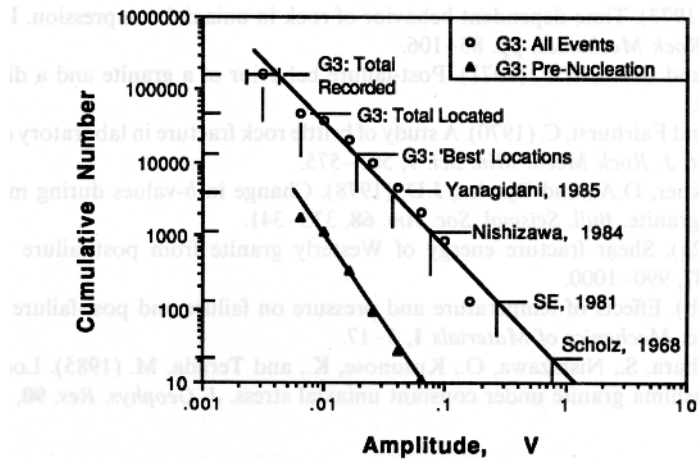


**Figure 13.** Cumulative number of AE events plotted vs. log (amplitude) for experiment G3. Open symbols, entire experiment; solid symbols, pre-nucleation events. Of 165117 events detected, 45713 were located with  $TT^{rms} < 5\mu s$ . Of these, approximately 19000 had adjusted amplitudes  $> 15$  mV and  $TT^{rms} < 1\mu s$ . These events were considered to have accurate locations and were used in the analysis. Numbers of events analyzed by other authors are plotted for comparison.

While this yield may at first seem low, it must be remembered that the location inversion routing requires good arrivals at all six transducers. If the first arrival is missed at any station owing, for example, to attenuation or to location of a station along a nodal plane of the radiation pattern, the location procedure will fail. Since most events have small amplitudes, this type of error will occur frequently. One way to improve the event yield is to have a denser array of stations, which we intend to incorporate in the next generation of acquisition system. To insure that we had strong first arrivals and therefore good timing accuracy, we culled the set of located events to approximately 19 000 large-amplitude events. Thus, we ultimately used only 11% of the recorded events in our detailed analysis, although the amplitude and travel-time residual criteria used to select events were precisely defined. As we will show, this yield ratio of usable events compares very favorably to those reported for hand-picked location studies.

To compare our results to hand-picked arrival-time data from other studies, we will assume, for the sake of argument, that the number and distribution of AE events occurring in each deformation experiment are similar to the G3 results shown in Figure 13. An early and well-known AE study was published by Scholz (1968), in which he reported microcrack localization based on 22 selected events (shown near bottom of Figure 13). These represent a small fraction, indeed, of the thousands of events that occurred during that experiment. Sondergeld and Estey (1981) detected 3360 events of which they located 116, presumably choosing the largest-amplitude events for their analysis. Even so, these represent a significantly smaller sampling than do our results. Nishizawa et al. (1984) located over 1000 events and, after considerable man-hours of work, Yanagidani et al. (1985) located 3933 hypocenters. These last two studies begin to approach our results in terms of sheer number of locations. Sondergeld and Estey, Nishizawa, and Yanagidani were also interested in analyzing first motions to obtain fault-plane solutions. In this case, inspection of the waveform is advised, although with more sophisticated techniques, automatic determination of first motion polarity should be possible. A similar assessment

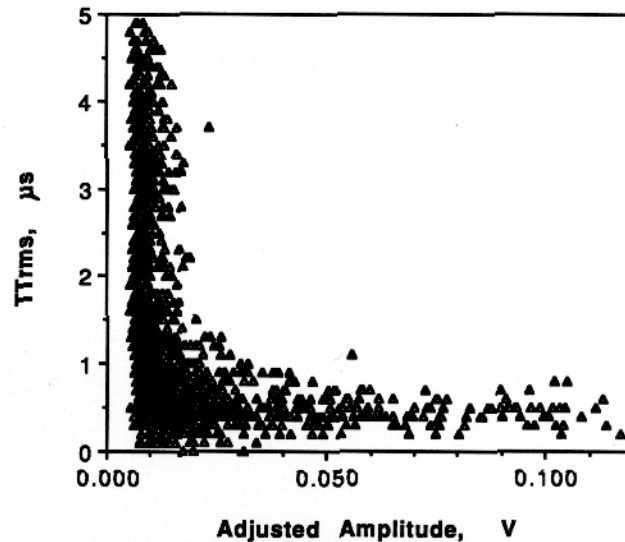


**Figure 14.** Distribution of  $TT^{rms}$  plotted as a function of event amplitude (adjusted to 10 mm from source) for 1600 events recorded in experiment G3. Above  $\sim 15$  mV, residuals cluster below  $1 \mu\text{s}$ , indicating that the first arrival is picked reliably for these events. Below 15 mV, residuals blow up, indicating that first arrivals are not picked reliably at all stations for these events.

can be made concerning the approximately 1000 events located during a recently reported triaxial test of granite by House et al. (1989).

To further analyze the performance of our automatic P-picker, we plot  $TT^{rms}$  as a function of amplitude in Figure 14. For adjusted amplitudes greater than 15 mV, travel-time residuals cluster below  $1 \mu\text{s}$ . Smaller-amplitude events give much larger residuals. This result indicates that below 15 mV the P-picker frequently misses the first arrival at one or more stations. However, above this cutoff, first arrivals were picked reliably at all transducers and for a typical P-wave velocity of 5 km/s would result in location errors of approximately  $\pm 2$  mm. This value is based on a formal maximum-likelihood estimate using actual transducer locations and events occurring in the central region of the sample. The fact that large-amplitude events give residuals that cluster at  $0.4 \mu\text{s}$  indicates a small systematic error in locating events in this segment of the experiment. This error could be the result of, for example, a 5% error in determination of the velocity field, a systematic late pick of first arrivals at the most distant stations, or timing errors due to the finite size of the transducers (3.2 mm radius). We cannot eliminate any of these possible causes at this time. The systematic deviations of AE locations from the observed fault planes near the ends of the sample (Figures 7-11) are most likely the result of an improper determination of the velocity structure. We are currently investigating methods for improving these determinations. However, what is most important for the present analysis is the relative error in determining locations of neighboring events. The small scatter in event locations when viewed along-strike (Figures 7-9) confirms that this error is less than  $\pm 3$  mm. The automated threshold detector system we have used does, in fact, perform well when compared to hand-picked arrival schemes and is certainly adequate for the present analysis. A more sophisticated system, employing current technology, can be expected to perform even better.